Transactions of the Canadian Society
for Mechanical Engineering

Evaluation and Validation of a Multiphysics Finite Element Model for a Piezoelectric Energy Harvester

Journal:	*Transactions of the Canadian Society for Mechanical Engineering*
Manuscript ID	TCSME-2019-0283.R2
Manuscript Type:	Article
Date Submitted by the Author:	01-Nov-2020
Complete List of Authors:	Melro, Andrew; Lakehead University, Mechanical Engineering Liu, Kefu; Lakehead University, Mechanical Engineering
Keywords:	Multiphysics, Energy harvesting, Vibration, Piezoelectric
Is the invited manuscript for consideration in a Special Issue? :	Not applicable (regular submission)

SCHOLARONE™
Manuscripts

Evaluation and Validation of a Multiphysics Finite Element Model for a Piezoelectric Energy Harvester

Andrew Melro, Kefu Liu[*]

Department of Mechanical Engineering, Lakehead University, Thunder Bay, ON P7B 5E1, Canada

[*]Corresponding author.
E-mail address: kliu@lakeheadu.ca

Abstract

This paper explores the applicability of using the multiphysics finite element method to model a piezoelectric energy harvester. The piezoelectric energy harvester under consideration consists of a stainless-steel cantilever beam attached by a piezoelectric ceramic patch. Two configurations are considered: one without a proof mass and one with a proof mass. Comsol Multiphysics software is used to simultaneously model three physics: the solid mechanics, the electrostatics, and the electrical circuit physics. Several key relationships are investigated to predict the behaviours of the piezoelectric energy harvester. The effects of the electrical load resistance and a proof mass on the performance of a piezoelectric energy harvester are evaluated. Experimental testing is conducted to validate the results found by the finite element model. Overall, the results from the finite element model closely match those from the experimental testing. It is found that increasing the load resistance of the piezoelectric energy harvester causes an increase in voltage across the load resistor, and matching the impedance yields the maximum power output. Increasing the proof mass reduces the fundamental frequency that results in an increase of the displacement transmissibility and the impedance matched resistance. The study shows that the multiphysics finite element method is effective to model piezoelectric energy harvesters.

Keywords

Multiphysics, Energy Harvesting, Vibration, Piezoelectric

2

1   Introduction

The aim of vibration energy harvesting is to harness ambient energy from the environment, which can be beneficial for low power consumption devices in many applications (Lynch and Loh 2006, Beeby, et al. 2006, Bowen, et al. 2014). For example, vibration energy harvesting is increasingly important in the field of structural health monitoring (SHM) in the pursuit of stand-alone self-powered sensors. The use of wireless sensor networks is attractive when communicating data over relatively large distances, such as in an aircraft or high-rise buildings, to reduce costs associated with coaxial cables (Lynch and Loh 2006, Beeby, et al. 2006, Bowen, et al. 2014). These sensors are powered by batteries that must be replaced once depleted. Incorporating energy harvesting into the design of a wireless sensor allows it to be stand-alone and self-powered, thus reducing the cost of battery replacement.

A system may experience either free vibration due to an initial disturbance or forced vibration due to persistent excitation. When the system experiences free vibration, its mechanical energy is dissipated through internal/external resistance (i.e. damping) in the form of heat. When subjected to forced harmonic excitation, the system continues to oscillate throughout the duration of the applied load, which may not be desired. In some cases, vibration energy harvesters attempt to serve a dual purpose of vibration suppression and energy scavenging (Xie, et al. 2013). Vibration suppression increases the desirability of utilising vibration energy harvesters.

Implementation of vibration energy harvesting requires the transformation of mechanical energy into electrical energy. This can be achieved in several ways, including electromagnetic, electrostatic, and piezoelectric. The main advantage of piezoelectric energy harvesters (PEHs) over electromagnetic or electrostatic energy harvesters is their greater volume figure of merit, which compares transducer performance as a function of their size (Mancelos, et al. 2014).

Many methods have been used to investigate the performance of PEHs, including uncoupled methods, equivalent electric circuit methods, and advanced modelling analyses (Zhu, et al. 2009). In (Lefeuvre, et al. 2005), the uncoupled method was employed to study the performance of three piezoelectric processing circuits. The work presented in (Shu and Lien 2006) showed that the uncoupled method did not yield accurate results when the energy harvesting device had a significant electromechanical coupling. In (Yang and Tang 2009, Liu 2011), the equivalent electric circuit method was used to investigate the performance of PEHs. However, this method typically led to an unconservative depiction of the power output of the PEHs (Zhu, et al. 2009). In (Lu, et al. 2004), an analytical model was proposed to study the behaviours of a cantilever PEH, including the effects of the electromechanical coupling of the device. The study reported in (Guyomar, et al. 2005) proposed a non-linear synchronized switch harvesting on inductor, which showed significant increases in power output of a PEH with high electromechanical coupling.

The geometry of a cantilever bimorph PEH with a proof mass was investigated in (Gallina and Benasciutti 2013). The authors employed a finite element (FE) model to compare the performance of rectangular and trapezoidal beam geometries without consideration of the piezoelectric material strength and experimental validation. The work reported in (Zhang, et al. 2013) investigated the impact of the proof mass on the fundamental frequency, the displacement amplitude, and the open-circuit voltage of a cantilever bimorph PEH. The results from an analytical and an FE model were compared with the experimental ones. An extensive

3

investigation on the numerical optimization of certain geometric parameters of a cantilever PEH was conducted in (Zhu, et al. 2010), presenting many relationships and recommendations for the PEH parameters. A novel meandering PEH was proposed in (Berdy, et al. 2012). The authors used FE models to show the improved performance of the meandering PEH compared to other designs. A new electromechanical FE modelling for a cantilevered piezoelectric energy harvester was developed in (Lumentut and Howard 2014). The proposed modelling process encompasses five major solution techniques. The study validated the FE modelling results with an experimental study. This modelling process was extended in (Lumentut and Howard 2016) to study the modal damped vibration energy harvesters with arbitrary proof mass offset. The FE modelling results were compared with those from the analytical closed-form boundary value technique. An experimental validation was conducted. On the other hand, in recent years, there has been a significant advance in commercial multiple physics FE software packages. They provide a great assistance in research and design of various multiphysics systems.

The main objective of the present paper is to explore the capability of a commercially available software package: Comsol Multiphysics. For this purpose, a cantilever beam attached by a piezoelectric ceramic patch is used as a PEH. A multiphysics FE model of the PEH is developed using Comsol Multiphysics. The performances of the PEH with or without a proof mass are investigated in terms of the fundamental frequency, transmissibility function, voltage, and power output of the PEH. Further, the effects of the load resistance on the power output of the PEH are investigated for both the configurations. An experimental study is conducted to validate the simulation results. The remainder of this paper is organized as follows. The design parameters of the PEH are presented in Section 2. The FE model is detailed in Section 3. The experimental testing apparatus is introduced in Section 4. The results are presented and discussed in Section 5, and the concluding remarks are made in Section 6.

2   Piezoelectric Energy Harvester Design

Figure 1 shows the geometry of a cantilever beam (grey), a piezo-ceramic patch (green) and a proof mass (orange). The proof mass is a magnet with a mass of 29 g, which can be attached or removed from the beam when required. The piezo-ceramic patch is glued to the stainless-steel beam using the 3M electrically conductive adhesive transfer tape 9707. Table 1 lists the material properties of the stainless-steel beam and proof mass. Only the density of the proof mass is known, thus, the remaining properties are assumed to be the same as the stainless-steel material. This assumption is reasonable, since the deformation of the proof mass is insignificant, and it has a negligible impact on the stiffness of the beam. The structural material properties of the adhesive tape are not provided by the manufacturer (3M n.d.). Further, the adhesive tape is assumed to have a negligible impact on the PEH and is not considered in the FE model.

Table 1: Stainless-steel beam and proof mass material properties

Stainless-steel Young's Modulus	200 GPa
Stainless-steel Density	8,000 kg/m^3
Stainless-steel Poisson's Ratio	0.29
Proof mass Young's Modulus	200 GPa
Proof mass Density	8,200 kg/m^3
Proof mass Poisson's Ratio	0.29

The piezo-ceramic material used is the PZT-5H manufactured by Steminc. Only the selected material property components are given by the piezo-ceramic material manufacturer. Specifically, the piezoelectric coefficients d_{33} and d_{31}, the elastic compliance components s_{11} and s_{33}, and the dielectric permittivity component e_{33} are available. Thus, the absent material properties are provided by the PZT-5H material built in Comsol, which is modified to suit the material property components given by the manufacturer where available. It can also be assumed that $s_{11} = s_{22}$, $s_{13} = s_{23}$, $s_{44} = s_{55}$, $d_{31} = d_{32}$, and $d_{15} = d_{24}$, according to (Sirohi and Chopra 2000). Thus, the material properties of the PZT-5H are defined as follows:

$$\mathbf{d} = \begin{bmatrix} 0 & 0 & 0 & 0 & 7.41 \times 10^{-10} & 0 \\ 0 & 0 & 0 & 7.41 \times 10^{-10} & 0 & 0 \\ -2.7 \times 10^{-10} & -2.7 \times 10^{-10} & 6 \times 10^{-10} & 0 & 0 & 0 \end{bmatrix} (\text{C/N})$$

$$\mathbf{s} = \begin{bmatrix} 1.39 \times 10^{-11} & -4.78 \times 10^{-12} & -8.45 \times 10^{-12} & 0 & 0 & 0 \\ & 1.39 \times 10^{-11} & -8.45 \times 10^{-12} & 0 & 0 & 0 \\ & & 1.89 \times 10^{-11} & 0 & 0 & 0 \\ & & & 4.35 \times 10^{-11} & 0 & 0 \\ & \text{Sym.} & & & 4.35 \times 10^{-11} & 0 \\ & & & & & 4.26 \times 10^{-11} \end{bmatrix} (\text{1/Pa})$$

$$\mathbf{e} = \begin{bmatrix} 3,130 & 0 & 0 \\ & 3,130 & 0 \\ \text{Sym.} & & 3,500 \end{bmatrix}$$

The density and quality factor of the piezo-ceramic material are 7,800 kg/m^3 and 80, respectively.

3   Finite Element Model

The FE model is developed using the Comsol Multiphysics version 5.2a. The numerical solvers use the default settings. In the interest of computational efficiency, the PEH is modelled in 2D using the plane strain approximation. The adhesive has a thickness of 50 μm, which is much thinner than the piezo-ceramic and stainless-steel beam. Modelling the adhesive tape would require a significant increase in the number of elements used in the model for an insignificant impact on the results. Further, the adhesive tape has an electric resistance less than 0.5 Ω for a 2 mm x 5 mm area. This is equivalent to an electrical resistance of less than 6.25 Ω for the PEH considered in this work, which is insignificant compared to the load resistances.

Therefore, the adhesive tape is neglected in modelling. The FE model is explained below, including mesh design, physics and study, boundary conditions, and post-processing.

Figure 2 shows the general geometry of the FE model. The proof mass used for the actual PEH, shown in Figure 1, is cylindrical in shape which cannot be modelled in 2D. Instead, the FE model represents the proof mass as two square cross-section rectangular prisms which span the out-of-plane width of the stainless-steel beam. The cross-sectional area of the proof mass in the FE model is selected such that it has a total volume equivalent to the physical proof mass. This ensures that the total mass of the proof mass is approximately 29 g in the FE model.

3.1   FE Model Mesh

Since the FE model involves the coupling of mechanical and electrical physics, the number of degrees of freedom is inherently increased when compared with an FE model involving single physics. Thus, a computationally efficient model mesh is desired as the number of elements used is directly related to the model's degrees of freedom. For the PEH without the proof mass, the piezo-ceramic domain and the stainless-steel beam use one quadratic quadrilateral element through their thickness. Along their lengths, the piezo-ceramic domain and the stainless-steel beam use 50 and 532 quadratic quadrilateral elements, respectively. This yields a total of 582 elements, with an average and minimum element quality of 0.9899 and 0.8824, respectively. The PEH with the proof mass uses the same mesh for the piezo-ceramic domain and the stainless-steel beam. However, the proof mass domains are represented by quadratic triangular elements, generated by the software package with a normal mesh density. Using triangular elements is suitable as it is assumed that the proof mass will experience negligible bending stress. The software package automatically generates a mesh to ensure continuity with the smaller quadratic quadrilateral elements. The proof mass domains are represented by 244 quadratic triangular elements. This yields 826 total elements for the PEH with the proof mass FE model, with an average and minimum element quality of 0.9751 and 0.7802, respectively. Figure 3 shows the FE model mesh for the PEH with the proof mass, including detailed views of the piezo-ceramic domain, and the proof mass domain, to clearly illustrate the mesh elements. The FE model mesh of the PEH without the proof mass is the same, apart from the proof mass domains.

3.2   Physics and Study

The PEH for both the configurations require a dynamic multi-physics FE simulation to evaluate the voltage load dependence, impedance matching, and transmissibility function. The FE simulation includes the solid mechanics, the electrostatics, and the electrical circuit physics. Further, the multi-physics coupling for piezoelectric devices is used to couple the electro-mechanical physics interaction. A time dependent and a frequency dependent study are used to solve for the responses of the PEH.

The time dependent study is used to determine the transmissibility function of the PEH. The transmissibility function is found by a harmonic excitation sweep, corresponding to the frequency range used in the experiment, which is discussed in Section 4. The transmissibility function of each PEH configuration is evaluated at the impedance matched resistance. A time duration of 10 seconds is used to collect the time response for the PEH without the proof mass, where the final 2 seconds represent the steady state solution, used to compute the transmissibility ratio (TR) for each excitation frequency. It was difficult for the PEH with the proof mass to

6

achieve steady state operation. Thus, a 50 second time duration is used in an attempt to minimize the transient response, where the final 2 seconds are used to determine the TRs.

The frequency dependent study is employed to compute the voltage load dependence and impedance matching. Although this could be done with a time dependent study, the frequency dependent study is computationally efficient by comparison since the software solves the steady state solution directly. Furthermore, the frequency dependent study is suitable in this case since the output from the PEH is determined by the strain energy of the piezo-ceramic material. Thus, the relative displacement of the input and output locations are not necessary to determine the voltage and power output.

To determine the voltage load dependence and impedance matching, an auxiliary sweep of the load resistance is performed. The resistance is varied between a range of 500 Ω - 3 MΩ for the PEH without the proof mass, and 500 Ω - 10 MΩ for the PEH with the proof mass. The PEH with the proof mass requires a higher resistance for impedance matching, which is discussed in Section 5.2.

3.3   Boundary Conditions

The boundary conditions for each physics module are discussed in the following. For both PEH configurations, the boundary conditions are the same. However, the settings for some of the boundary conditions are different to suit each configuration. For example, the damping model for each PEH configuration must be tuned individually.

The solid mechanics physics module includes the material models for the PEH components. The initial displacement and velocity are set to zero ($\mathbf{u}(0) = \mathbf{0}$, $\partial\mathbf{u}/\partial t(0) = \mathbf{0}$). The linear elastic material model is applied to the stainless-steel beam and proof mass domain, while the piezoelectric material model is applied to the piezo-ceramic domain. The piezoelectric material allows the user to define the piezoelectric constitutive relation. Since the material properties provided by the manufacturer are based on the strain-charge form, it is used as the constitutive relation for the piezoelectric material. Within the linear elastic and piezoelectric material models, the Rayleigh damping and dielectric loss are defined, respectively. The dielectric loss is selected as 1.25%, which is the inverse of the piezo-ceramic material quality factor.

The PEH is intended to operate at its fundament frequency. Thus, the Rayleigh damping is tuned using only the fundamental frequency. Comsol suggests that the Rayleigh damping can be modified to represent an equivalent viscous damping model at the resonant frequency by considering only the stiffness proportional term (Comsol 2016). This gives a significantly overdamped displacement response. Another approach is to consider only the mass proportional term. According to (Trombetti and Silvestri 2007), this is equivalent to connecting dampers to lumped masses in a multiple-degree-of-freedom structure, and fixing each damper to a fixed location, such as the ground. Further, according to (Trombetti and Silvestri 2007) the mass proportional contribution to the Rayleigh damping is dominant in the low frequency range and is a good estimate of Rayleigh damping in this range. Conversely, the mass proportional term tends to zero in the high frequency range, and the stiffness proportional term is dominant. Since the PEH operates in the low frequency range, only the mass proportional term is used. Using this approach, the Rayleigh damping is modified as follows:

$$\mathbf{C} = \mu\mathbf{M} \tag{2}$$

$$\mu = 4\pi\zeta_n f_n \tag{3}$$

In equation (3) the subscript n is equal to 1 since the fundamental frequency of the PEH is used.

The time dependent study requires different boundary conditions from those for the frequency dependent study in terms of applied loads and constraints. A prescribed displacement, Figure 4, is applied to the base of the PEH in the time dependent study to simulate base excitation. The prescribed displacement is sinusoidal, having an amplitude of 10 mm, and a driving frequency that is incremented in the frequency sweeping range. For the frequency dependent study, a fixed constraint and body load replace the prescribed displacement. The fixed constraint, Figure 4, is applied to the base of the PEH structure. The body load is applied to all the PEH domains, and the applied load is described in terms of g-force. The voltage output across the load resistor of the PEH scales linearly with the applied body load. Since the applied g-force from the experiment is not measured, the FE model initially uses a body load of 1 g-force. The voltage corresponding to the impedance matched resistance is then scaled by the experimental one to determine the g-force which gives voltage and power output results comparable to the experiment. This yields a body load of approximately 1.2 x 10^{-3} g-force and 1.0 x 10^{-3} g-force for the PEH without the proof mass and with the proof mass, respectively.

The electrostatics boundary conditions are the same for both the time dependent and frequency dependent study. The initial electric potential is set to zero (V(0) = 0). The boundary conditions applied to the PEH are the ground and terminal nodes. The ground node is applied to the top of the piezo-ceramic domain, Figure 5 (a), while the terminal node is applied at the interface of the piezo-ceramic and stainless-steel beam domain, Figure 5(b). Within the terminal settings, the terminal type is selected as a circuit, such that the terminal can be used by the electrical circuit physics.

The electrical circuit module allows for an electrical circuit to be linked to the FE model. The electric circuit is the same for both the time dependent and frequency dependent study. The electrical circuit includes a ground node, a resistor, and an external terminal. The resistance of the load is varied, which is used to determine the voltage load dependence and the output power load dependence. The external terminal reads the electric potential from the electrostatics terminal output. Then the electric circuits module simulates the voltage drop across the load resistor.

3.4 Post-Processing

The TR function relates the base displacement to the displacement measured at a location of interest, over a given frequency range. The transmissibility ratio function is found as follows:

$$TR(\omega) = \frac{x_o(\omega)}{x_i(\omega)} \tag{4}$$

where $x_o(\omega)$ and $x_i(\omega)$ represent the output displacement, and base displacement, respectively, at a given excitation frequency, ω. After the multiphysics simulation in the time dependent study is conducted, the root mean squared (RMS) values of the base displacement and the displacement

8

of the free end of the beam are used to compute the transmissibility ratio function for each PEH configuration.

To evaluate the voltage load dependence, the voltage output across the load resistor is evaluated for each resistance used in the frequency sweep for the frequency dependent study. Since the resistor is not discretely modelled, a global evaluation of the resistor from the electrical circuit module is used. The absolute voltage across the resistor is measured. The voltage output is necessary to compute the power output of the PEH to perform impedance matching. The power output of the PEH for each resistance value is computed as follows:

$$P = \frac{V^2}{R} \tag{5}$$

where V and R represent the voltage across the load resistor and resistance of the load resistor, respectively. Impedance matching is performed by plotting the power output versus load resistance to find the resistance which corresponds to the maximum power output.

4   Experimental Validation

To validate the results of the FE multiphysics simulation, an experimental study is conducted. A PEH specimen is made by following the specifications of the FE model. Figure 6 shows the experimental setup. The apparatus is mounted on a shaking table that is driven by a modal shaker (The Modal Shop, 2100E11) through a stinger. An amplifier is used to amplify the exciting signal to the shaker. The displacements of the base and the beam at a specified location are measured by two optical position sensors (Wenglor, CP24MHT80), respectively. A power supply provides power to the optical position sensor. Lastly, a data acquisition unit (Brüel & Kjær, 2827-002) is used to facilitate communication between a computer and software. The sampling frequency of the experiment is 512 Hz so that a sample is collected every 1.953 ms.

Prior to recording data, the modal shaker is set at the driving frequency for approximately ten seconds to minimize the transient response. Then, data is recorded for a two-second time duration. The collected signals are processed using a low-pass Butterworth filter with the cut-off frequency that equals to $f + 6$ Hz where f is the exciting frequency in order to remove noise. The selected filter order is 8. Zero padding, similar to a rectangular window, is used to prevent spectral leakage and improve the frequency spectrum resolution. Zeros are appended to the measured data by sixteen times the number of data samples. The time signals are transformed to the frequency domain by the Fast Fourier Transform.

Figure 7 shows a close view of the energy harvesting circuit consisting of a variable resistor that is connected to the leads of the piezo-ceramic patch. The voltage response across the variable resistor is recorded by the data acquisition unit. To determine the voltage load dependence and impedance matching, the PEH is excited at its fundamental frequency. The fundamental frequency of the PEH without the proof mass and with the proof mass determined by the FE model is 6.7 Hz and 3.4 Hz, respectively. Once the PEH's response reaches steady state, the voltage output across the resistor is recorded over a time duration of two seconds. This process is conducted for load resistances of 500 Ω, 1 kΩ, 2 kΩ. 5 kΩ, 10 kΩ, 20 kΩ, 50 kΩ, 100 kΩ, 200 kΩ, 500 kΩ, 1 MΩ, 2 MΩ, and 3 MΩ for the PEH without the proof mass, while the PEH with the proof mass also includes load resistances of 5 MΩ, and 10 MΩ.

The RMS values of the processed base and tip time response at a given driving frequency are computed to evaluate the transmissibility ratio according to equation (3). To measure the transmissibility function, a frequency sweep excitation is conducted. With the electrical circuit closed with the impedance matched load resistor, the PEH is subjected to a harmonic base motion and the steady state responses are measured. The driving frequency ranges of the PEH without the proof mass and the PEH with the proof mass are between 4 Hz – 10 Hz and 3 Hz – 4 Hz, respectively. The frequency resolutions of the PEH without the proof mass are 0.25 Hz and 0.10 Hz when far from and near the resonant frequency, respectively. The frequency resolution of the PEH with the proof mass is 0.05 Hz throughout the frequency sweep. The transmissibility function is then established by plotting the transmissibility ratios at their corresponding driving frequency.

5　Results and Discussion

5.1　Mode Shapes

The first four normalized mode shapes determined by the FE model for the PEH without and with the proof mass are shown in Figure 8 and Figure 9, respectively. The mode shapes for the PEH without the proof mass correspond to the following respective frequencies: 6.7 Hz, 41.0 Hz, 113.0 Hz, and 218.1 Hz. The mode shapes for the PEH with the proof mass correspond to the following respective frequencies: 3.4 Hz, 31.4 Hz, 95.2 Hz, and 190.6 Hz. Further, the first four normalized strain mode shapes are illustrated in Figure 10 and Figure 11, respectively.

5.2　PEH Voltage Load Dependence and Impedance Matching

Figure 12 (a) shows the voltage load dependence, determined experimentally and by the FE model, of the PEH without the proof mass. In general, the voltage load dependence determined by the FE model is in close agreement with that from the experiment. The voltage output tends to increase with an increasing load resistance for the resistance sweep considered. The voltage load dependence curves, determined by the experiment and the FE model, are concave upwards up to the inflection point at a load resistance of 1 MΩ, where the curve becomes concave downwards. The maximum voltage outputs determined by the experiment and the FE model are 0.517 V and 0.554 V, respectively.

Impedance matching is an important consideration in the performance of a PEH, as it maximizes the power output (Frenzel 2011). By varying the resistive load on the circuit and computing the power output of each corresponding resistance, the impedance matched resistance is found, which corresponds to the maximum power output. Figure 12 (b) shows the impedance matching curves for the PEH without the proof mass. The impedance matching curve determined by the FE model compares favorably with the experimental one. In both the experimental and the FE results, the power output reaches a maximum at a load resistance of 1 MΩ. This load resistance is the impedance matched resistance of the PEH without the proof mass. The maximum power output magnitude measured by the experiment of 144 nW is the same as that determined by the FE model. Of course, this is expected since the FE model body load is scaled based on the voltage output at the impedance matched resistance.

The voltage load dependence, determined experimentally and by the FE model, of the PEH with the proof mass are shown in Figure 13 (a). The voltage load dependence determined by the FE model compares well with the experiment, showing a similar trend. Like the voltage

load dependence from Figure 12 (a), increasing the load resistance causes an increase in the voltage output across the resistor. In this case, the inflection point location in the voltage load dependence curve differs between the experiment and the FE model. The inflection point of the voltage load dependence curve determined by the experiment is located at a load resistance of 2 MΩ, whereas the FE model shows the inflection point at a load resistance of 3 MΩ. The FE model uses higher load resistances in the resistance sweep than the experiment. This is done to show the general trend of the voltage load dependence curve determined by the FE model beyond the inflection point, which is useful for impedance matching. Thus, the voltage outputs, determined experimentally and by the FE model, at a load resistance of 3 MΩ are 0.170 V and 0.188 V, respectively.

The impedance matching curves for the PEH with the proof mass, determined experimentally and by the FE model, are shown in Figure 13 (b). The overall trend of the impedance matching curve determined by the FE model compares well with that from the experiment. The maximum power outputs correspond to the locations of the inflection points from the voltage load dependence curves. The impedance matched resistance determined by the experiment is 2 MΩ, which gives a maximum power output of 11.5 nW. The impedance matched resistance determined by the FE model is 3 MΩ, giving a maximum output of 11.8 nW. In this case, the maximum power outputs are different, since the FE body load is scaled by the voltage corresponding to the experimental impedance matched resistance to ensure the same power output at 2 MΩ.

5.3   PEH Transmissibility Functions

The measured damping ratios of both the PEH configurations are listed in Table 2. The damping ratios are determined using the quadrature peak picking method. It can be seen that the damping ratio of the PEH without the proof mass is significantly larger than that of the PEH with the proof mass.

Table 2: PEH damping ratios.

PEH Configuration	Damping Ratio ζ_1
With the proof mass	6.675×10^{-3}
Without the proof mass	1.247×10^{-2}

Figure 14 (a) shows the transmissibility functions determined experimentally and by the FE model for the PEH without the proof mass. The transmissibility function determined by the FE model shows good agreement with that determined by the experiment. The fundamental frequency determined by the FE model is 6.7 Hz, whereas the experimental fundamental frequency is 6.5 Hz, giving a relative error percentage of approximately 3.08%. The transmissibility function magnitudes at the fundamental frequency determined by the FE model and the experiment are 72.07 and 69.03, respectively. These magnitudes are within an order of magnitude and give a relative error percentage of approximately 4.40%.

Figure 14 (b) shows the transmissibility functions determined experimentally and by the FE model for the PEH with the proof mass. In general, the transmissibility function determined by the FE model compares well with that by the experiment. However, the transmissibility function determined by the FE model is not as smooth as that by the experiment. Section 3.2

11

mentions that the time response of the PEH determined by the FE model did not reach steady state for some of the driving frequencies. This explains the poor smoothness of the transmissibility function determined by the FE model. The fundamental frequency found experimentally is 3.35 Hz, whereas the fundamental frequency determined by the FE model is 3.4 Hz, giving a relative error percentage of approximately 1.49%. The transmissibility function magnitudes at the fundamental frequency determined by the FE model and the experiment are 99.17 and 119.60, respectively, giving a relative error percentage of approximately 17.08%.

5.4   Impact of the Proof Mass

Comparing the transmissibility functions, determined experimentally, of both the PEH configurations leads to some key insights. Most obviously, the fundamental frequency of the PEH is directly impacted by the proof mass. This is useful for tuning the PEH to suit the exciting frequency of the ambient vibration. Ensuring that the PEH is excited at its fundamental frequency increases its power output, which is desired. Further, the transmissibility function magnitude at the fundamental frequency for the configuration with the added proof mass is larger than the magnitude for the configuration without the proof mass. Thus, for a given input displacement applied to both the PEH configurations, the configuration with the proof mass has a larger free end displacement, which should increase the strain energy of the piezo-ceramic material.

Interestingly, the maximum power output of the PEH without the proof mass is significantly larger than that of the PEH with the proof mass. Their respective impedance matched power outputs are 144 nW and 11.8 nW. This seems to conflict with the expected increase in piezo-ceramic strain energy caused by the added proof mass. However, this could be related to the mechanical power input, which may have been higher for the PEH without the proof mass. Since the mechanical power input was not measured experimentally, the FE model is used to estimate it. It is found that the simulation mechanical power input for the PEH without the proof mass and the PEH with the proof mass are 905 nW and 63.5 nW, respectively. These give respective efficiencies of 15.94% and 18.17%. Therefore, the increased efficiency of the PEH with the proof mass suggests that the low power output relative to the PEH without the proof mass is related to its mechanical power input. Of course, this requires experimental validation since the mechanical power input determined by the FE model is based on the scaled applied body load.

The proof mass tends to cause an increase in the impedance matched resistance. Comparing the impedance matching curves of both the configurations in Figure 12 (b) and Figure 13 (b), it can be seen that the impedance matched resistance without the proof mass is 1 MΩ, whereas the addition of the proof mass increases it to 2 MΩ. This suggests that increasing the proof mass could be a way to tune the impedance matched resistance of the piezo-ceramic material.

6   Conclusion

This paper has investigated the dynamic responses and output performances of a piezoelectric energy harvester (PEH) using a commercial multiphysics finite element software package: Comsol Multiphysics. Two configurations have been considered: the PEH without a proof mass and the PEH with a proof mass. The transmissibility functions, voltage load dependence, and impedance matching for each PEH configuration found by the FE model were

12

compared with those from the experiment. Overall, the results of the multiphysics FE simulation agree with those from the experiment. In particular, the transmissibility functions and fundamental frequencies determined by the FE models were validated by the experimental ones. However, further analysis should be done to validate the performance of the FE model with respect to the voltage load dependence, and impedance matching results, since the body load magnitude was scaled based on the experimental impedance matched output voltage. The study has shown that the multiphysics FE method is effective to model the behaviors of the PEH.

13

References

3M. n.d. 3M™ Electrically Conductive Adhesive Transfer Tape 9707. Available from 3m.com/3M/en_US/company-us/all-3m-products/~/3M-Electrically-Conductive-Adhesive-Transfer-Tape-9707?N=5002385+3294001412&rt=rud [accessed 24 May 2016].

Beeby, S.P., Tudor, M.J., and White, N.M. 2006. Energy harvesting vibration sources for microsystems applications. Meas. Sci. Technol. **17**(12): 175-195. doi:10.1088/0957-0233/17/12/R01.

Berdy, D.F., Srisungsitthisunti, P., Jung, B., Xu, X., Rhoads, J.F., and Peroulis, D. 2012. Low-frequency meandering piezoelectric vibration energy harvester. IEEE Trans. Ultrason. Ferroelectrics, Freq. Control. **59**(5): 846-858. doi:10.1109/TUFFC.2012.2269.

Bowen, C.R., Kim, H.A., Weaver, P.M., and Dunn, S. 2014. Piezoelectric and ferroelectric materials and structures for energy harvesting applications. Energy Environ. Sci. **7**: 25-44. doi:10.1039/C3EE42454E.

Comsol. 2016. Structural mechanics module user's guide. Comsol.

Frenzel, L. 2011. Back to basics: Impedance matching (part 1). Available from electronicdesign.com/communications/back-basics-impedance-matching-part-1 [Accessed 5 November 2017].

Gallina, M., and Benasciutti, D. 2013. Finite element analysis of optimized piezoelectric bimorphs for vibrational "energy harvesting". In Proceedings of the International CAE Conference. Lazise, Lago di Garda, 21-22 October 2013. pp. 1-4.

Guyomar, D., Badel, A., Lefeuvre, E., and Richard, C. 2005. Toward energy harvesting using active materials and conversion improvement by nonlinear processing. IEEE Trans. Ultrason. Ferroelectrics, Freq. Control **52**(4): 584-595. doi:10.1109/TUFFC.2005.1428041.

Lefeuvre, E., Badel, A., Richard, C., Petit, L., and Guyomar, D. 2005. A comparison between several vibration-powered piezoelectric generators for standalone systems. Sens. Actuators A **126**(2): 405-416. doi:10.1016/j.sna.2005.10.043.

Liu, H. 2011. Piezoelectric MEMS energy harvester for low-frequency vibrations with wideband operation range and steadily increased output power. J. Microelectromechanical Syst. **20**(5): 1131-1142. doi:10.1109/JMEMS.2011.2162488.

Lu, F., Lee, H.P., and Lim, S.P. 2003. Modeling and analysis of micro piezoelectric power generators for micro-electromechanical-systems applications. Smart Mater. Struct. **13**(1): 57-63. doi:10.1088/0964-1726/13/1/007.

Lumentut, M.F., and Howard, I.M. 2014. Electromechanical finite element modelling for dynamic analysis of a cantilevered piezoelectric energy harvester with tip mass offset under base excitation. Smart Mater. Struct. **23**: 095037 (24pp). doi:10.1088/0964-1726/23/9/095037.

Lumentut, M.F., and Howard, I.M. 2016. Parametric design-based modal damped vibrational piezoelectric energy harvesters with arbitrary proof mass offset: Numerical and analytical validations. Mech. Sys. Signal Process. **68-69**: 562-586. doi:10.1016/j.ymssp.2015.05.017.

Lynch, J.P., and Loh, K.J. 2006. A summary review of wireless sensors and sensor networks for structural health monitoring. Shock Vib. Dig. **38**(2): 91-128. doi:10.1177/0583102406061499.

Mancelos, N., Correia, J., Pires, L.M., Oliveira, L.B., and Oliveira, J.P. 2014. Piezoelectric energy harvester for a CMOS wireless sensor. In Technological innovation for collective awareness systems. DoCEIS 2014. IFIP Advances in Information and Communication Technology, vol 423. Edited by L.M. Camarinha-Matos, N.S. Barrento, R. Mendonça. Springer, Berlin, Heidelberg. pp. 470-477.

Shu, Y.C, and Lien, I.C. 2006. Analysis of power output for piezoelectric energy harvesting systems. Smart Mater. Struct. **15**(6): 1499-1512. doi:10.1088/0964-1726/15/6/001.

Sirohi, J., and Chopra, I. 2000. Fundamental understanding of piezoelectric strain sensors. J. Intell. Mater. Sys. Struct. **11**(4): 246-257. doi:10.1106/8BFB-GC8P-XQ47-YCQ0.

Trombetti, T., and Silvestri, S. 2007. Novel schemes for inserting seismic dampers in shear-type systems based upon the mass proportional component of the Rayleigh damping matrix. J. Sound Vib. **302**(3): 486-526. doi:10.1016/j.jsv.2006.11.030.

Xie, X.D., Wu, N., Yuen, K.V., and Wang, Q. 2013. Energy harvesting from high-rise buildings by a piezoelectric coupled cantilever with a proof mass. Int. J. Eng. Sci. **72**: 98-106. doi:10.1016/j.ijengsci.2013.07.004.

Yang, Y., and Tang, L. 2009. Equivalent circuit modeling of piezoelectric energy harvesters. J. Intell. Mater. Sys. Struct. **20**(18): 2223-2235. doi:10.1177/1045389X09351757.

Zhang, L., Williams, K.A., and Xie, Z. 2013. Evaluation of analytical and finite element modeling on piezoelectric cantilever bimorph energy harvester. Trans. Can. Soc. Mech. Eng. **37**(3): 621-629. doi:10.1139/tcsme-2013-0050.

Zhu, M., Worthington, E., and Tiwari, A. 2010. Design study of piezoelectric energy-harvesting devices for generation of higher electrical power using a couple piezoelectric-circuit finite element method. IEEE Trans. Ultrason. Ferroelectrics, Freq. Control. **57**(2): 427-437. doi:10.1109/TUFFC.2010.1423.

Zhu, M., Worthington, E., and Njuguna, J. 2009. Analyses of power output of piezoelectric energy-harvesting devices directly connected to a load resistor using a coupled piezoelectric-circuit finite element method. IEEE Trans. Ultrason. Ferroelectrics, Freq. Control. **56**(7): 1309-1318. doi:10.1109/TUFFC.2009.1187.

Figure Captions

Figure 1: PEH geometry with the proof mass (not drawn to scale).

Figure 2: Geometry of the PEH FE model with the proof mass.

Figure 3: PEH with the proof mass FE model mesh: (a) complete FE model mesh; (b) piezo-ceramic domain detail; (c) proof mass domain detail.

Figure 4: Prescribed Displacement and Fixed Constraint Boundary Conditions

Figure 5: Electrostatics Boundary Conditions: (a) ground node; (b) terminal node

Figure 6: Experimental apparatus.

Figure 7: PEH Experiment circuitry.

Figure 1: Normalized mode shapes of the PEH without the proof mass: (a) mode 1; (b) mode 2; (c) mode 3; (d) mode 4

Figure 2: Normalized mode shapes of the PEH with the proof mass: (a) mode 1; (b) mode 2; (c) mode 3; (d) mode 4

Figure 10: Normalized strain mode shapes of the PEH without the proof mass: (a) mode 1; (b) mode 2; (c) mode 3; (d) mode 4

Figure 11: Normalized strain mode shapes of the PEH with the proof mass: (a) mode 1; (b) mode 2; (c) mode 3; (d) mode 4

Figure 12: PEH performance without the proof mass: (a) voltage load dependence; (b) impedance matching.

Figure 13: PEH performance with the proof mass: (a) voltage load dependence; (b) impedance matching.

Figure 14: Transmissibility functions: (a) without the proof mass; (b) with the proof mass.

16
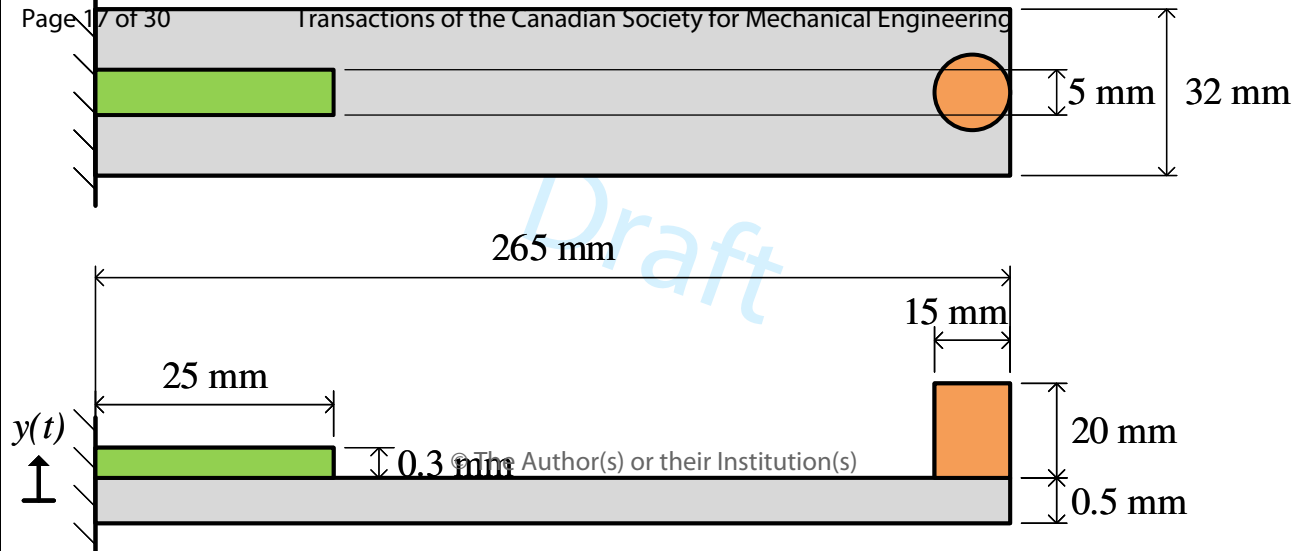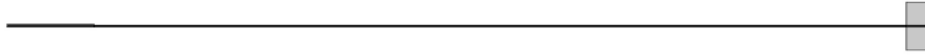
Figure 2: Geometry of the PEH FE model with the proof mass.

348x137mm (96 x 96 DPI)

(a)
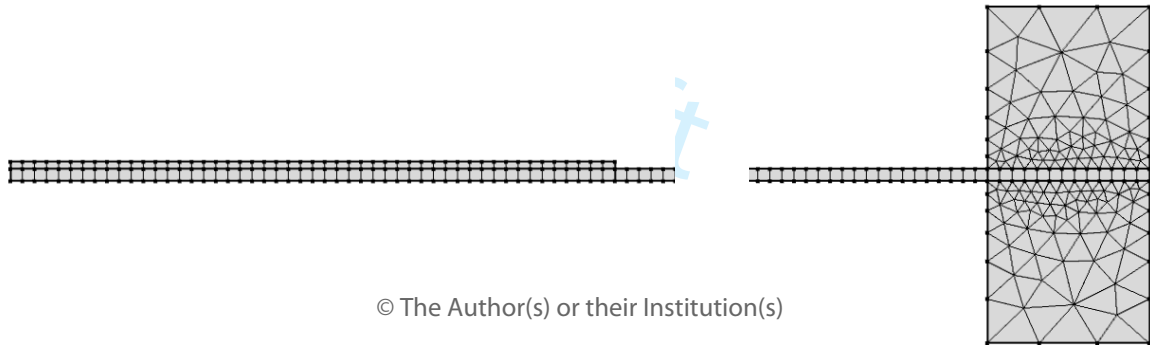
(b)   (c)

Figure 4: Prescribed Displacement and Fixed Constraint Boundary Conditions
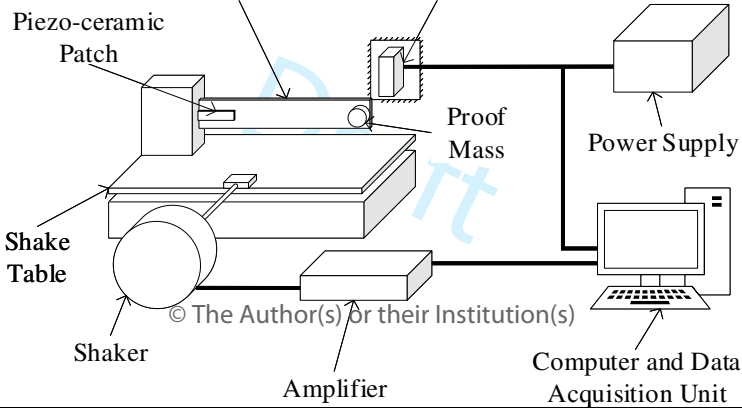
165x6mm (96 x 96 DPI)
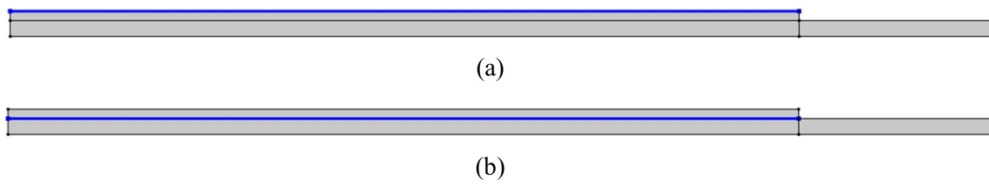
Figure 5: Electrostatics Boundary Conditions: (a) ground node; (b) terminal node
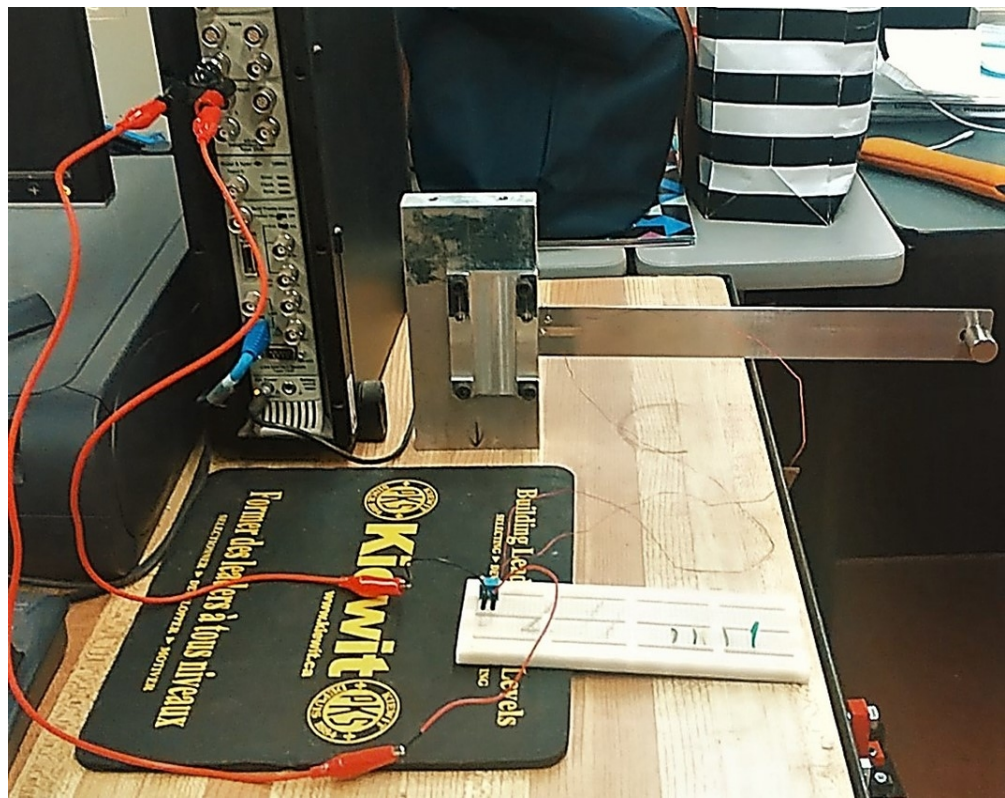
568x118mm (96 x 96 DPI)

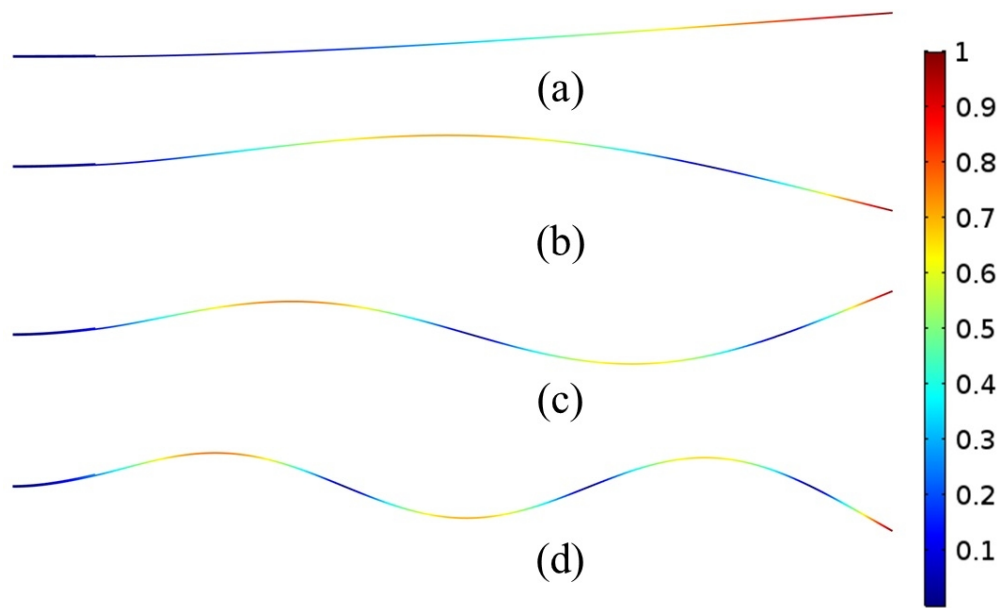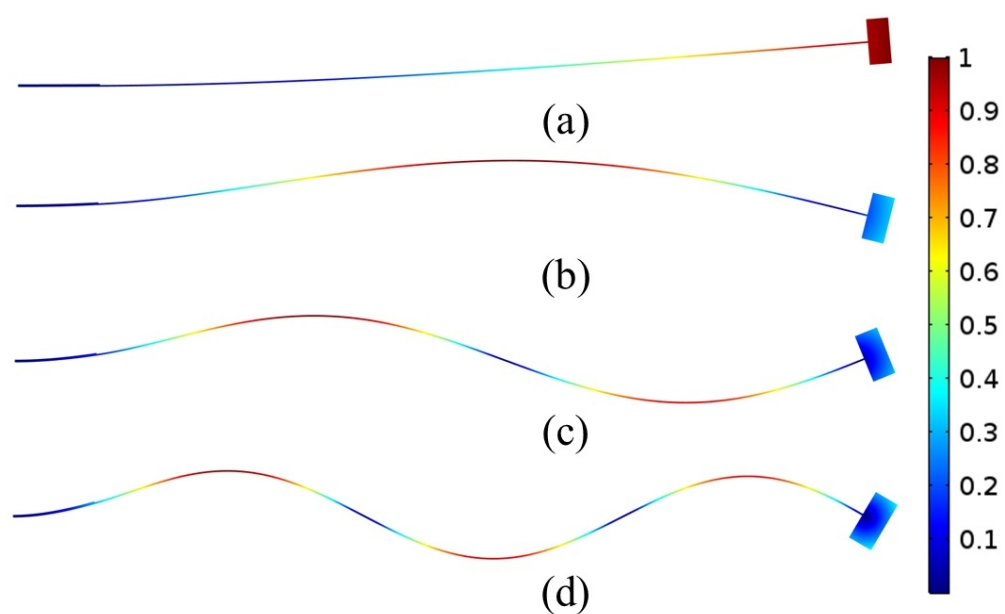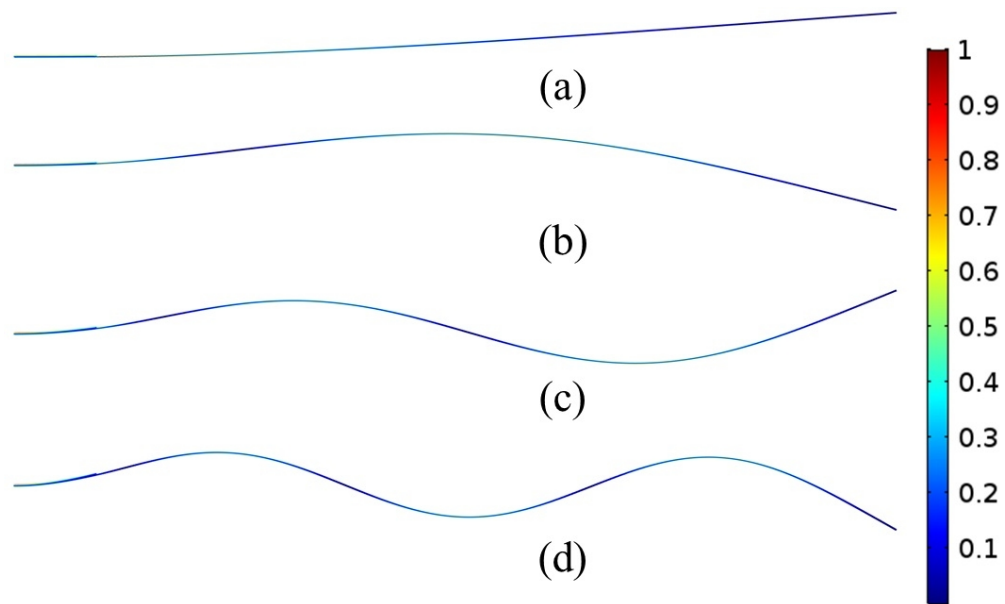Figure 7: PEH Experiment circuitry.

376x297mm (72 x 72 DPI)

Figure 8: Normalized mode shapes of the PEH without the proof mass: (a) mode 1; (b) mode 2; (c) mode 3; (d) mode 4
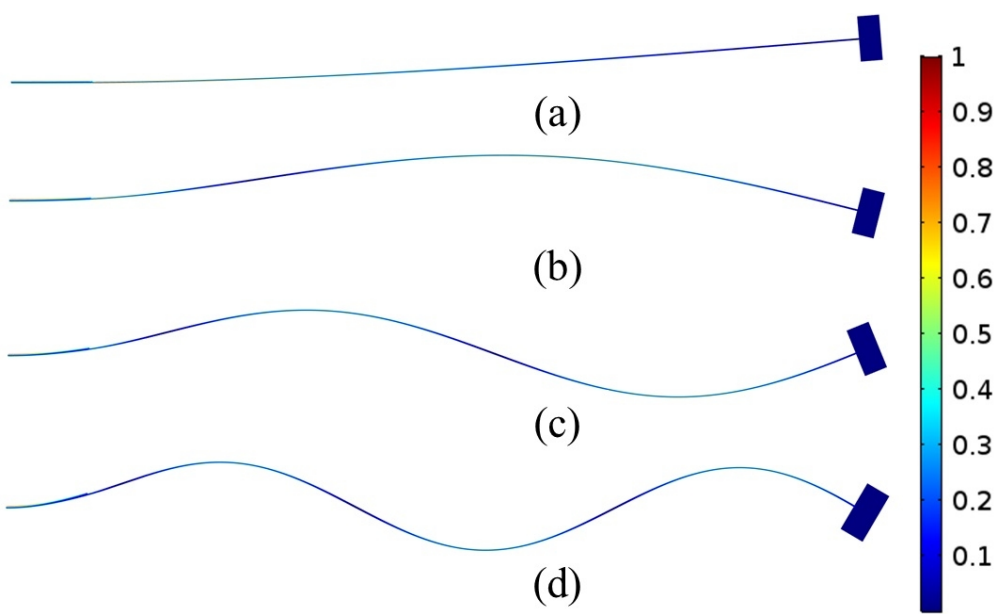
280x170mm (96 x 96 DPI)

Figure 9: Normalized mode shapes of the PEH with the proof mass: (a) mode 1; (b) mode 2; (c) mode 3; (d) mode 4

280x175mm (96 x 96 DPI)

Figure 10: Normalized strain mode shapes of the PEH without the proof mass: (a) mode 1; (b) mode 2; (c) mode 3; (d) mode 4

280x169mm (96 x 96 DPI)

Figure 11: Normalized strain mode shapes of the PEH with the proof mass: (a) mode 1; (b) mode 2; (c) mode 3; (d) mode 4
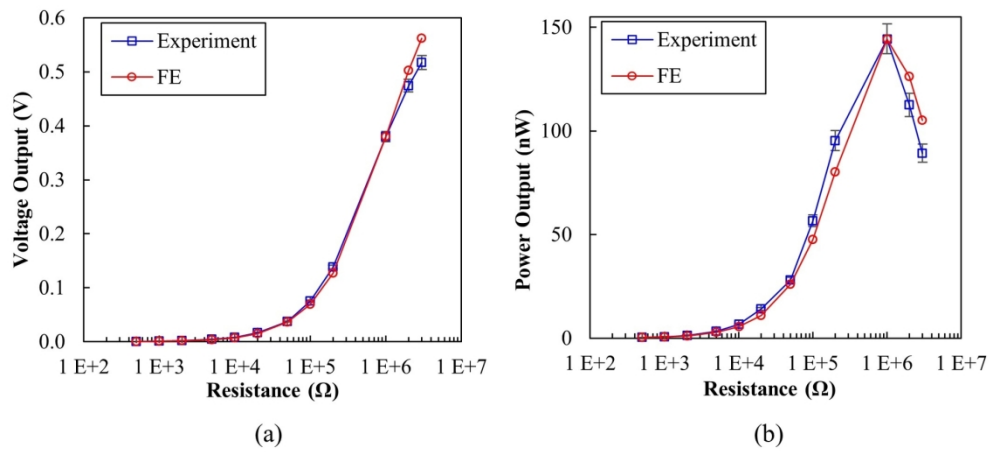
280x173mm (96 x 96 DPI)

Figure 12: PEH performance without the proof mass: (a) voltage load dependence; (b) impedance matching.
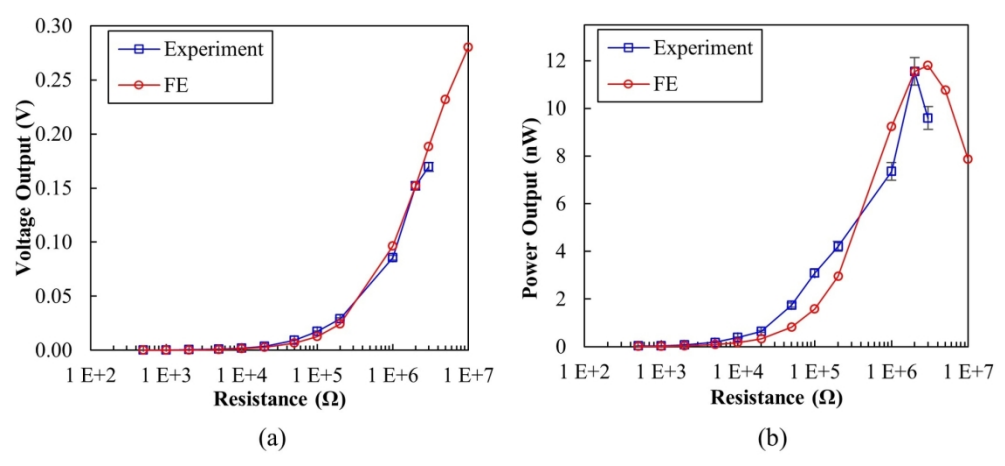
164x75mm (300 x 300 DPI)

Figure 13: PEH performance with the proof mass: (a) voltage load dependence; (b) impedance matching.
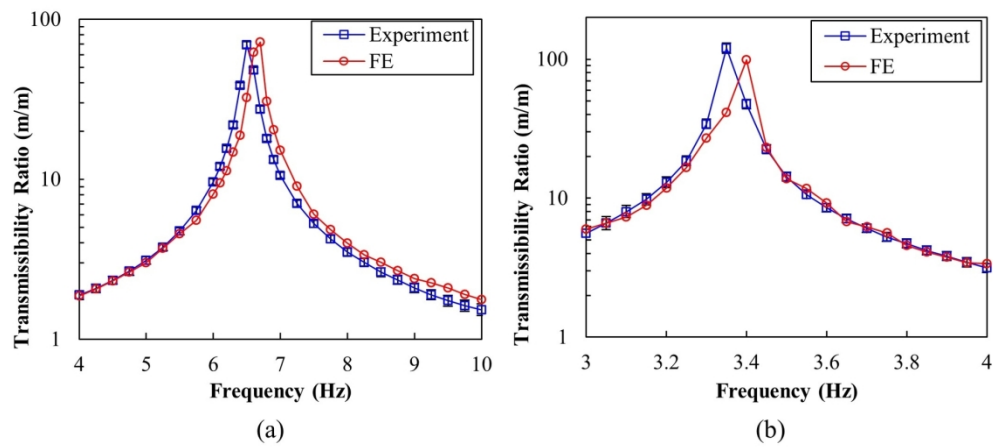
164x74mm (300 x 300 DPI)

Figure 14: Transmissibility functions: (a) without the proof mass; (b) with the proof mass.

164x74mm (300 x 300 DPI)